# Present-day crustal deformation based on an interpolated GPS velocity field in the collision zone of the Arabia-Eurasia tectonic plates

ASGHAR RASTBOOD[1], MILAD SALMANIAN[2] AND MASOUD MASHHADI HOSSAINALI[2]

1 Department of Surveying Engineering, Faculty of Civil Engineering, University of Tabriz, Tabriz, Iran (arastbood@tabrizu.ac.ir)

2 Faculty of Geodesy and Geomatics Engineering, K.N. Toosi University of Technology, Tehran, Iran

*Received: October 1, 2023; Revised: May 17, 2024; Accepted: July 24, 2024*

## ABSTRACT

*The oblique collision zone of Arabia-Eurasia is a seismically active region with complex crustal deformation patterns. While GPS measurements provide valuable data, their sparse distribution limits our understanding of the full extent of deformation. This study addresses this limitation by using a robust interpolation method for GPS velocity data in the collision zone. We utilized biharmonic splines to interpolate horizontal components of sparse GPS velocity data independently and in a coupled manner by altering Poisson ratio. This method is an effective means of interpolating sparse vector data in cases where deformation mechanics can be explained by elasticity principles. The interpolation process included fitting trends to the input data, calculating residuals, and analyzing them. The prediction process consisted of trend and spline fitting stages. We interpolate horizontal GPS velocities onto a standard geographic grid with a 30-minute interval, excluding data points with significant deviation. The data was partitioned into training and testing subsets, with the training set used for calibration and the testing set for evaluation of the interpolation method. Our analysis revealed an irregular spatial distribution of crustal movement. The northern component of the velocity field consistently points towards Eurasia and is greater than the eastern component. The amplitude of the northern component decreases from south to north and from west to east, indicating variations in deformation intensity. The eastern component exhibits a change in direction, moving westward in the western half of Iran and eastward in the eastern half, with a reversed trend in the north. This change in direction highlights the presence of solid blocks within the collision zone. Undeformed regions, major faults, convergence deformation, and compressing high-elevation regions are also observed in the collision zone. These findings provide a detailed picture of present-day crustal deformation in the Arabia-Eurasia collision zone, enhancing our understanding of the collision process.*

Keywords: biharmonic spline, interpolation, Green functions, horizontal GPS velocity field, Arabia-Eurasia


© 2024 Inst. Geophys. CAS, Prague, Czech Republic

## 1. INTRODUCTION

The surface displacement of the Earth's crust is an inherently continuous phenomenon, and each position of the Earth's surface has some value of this displacement, and it is possible to measure it on the Earth's surface. Continuous data, including displacement, cannot be measured at all points of the surface due to their continuity, so they are generally collected in sample form using geodetic tools. Surface displacement measurements on the Earth's surface exhibit a significant amount of scattering and heterogeneous distribution. This is particularly evident in displacement measurements obtained via the Global Positioning System (GPS), as the availability of ground stations limits the spatial coverage of these measurements. Despite offering high temporal resolution and precision, the spatial scattering of GPS data poses a challenge for data processing methods that require a regular, uniform grid for accurate analysis, such as the Fourier transform, directional derivatives (*Gonzales and Woods, 2018*), or displacements from GPS observations that are commonly utilized as inputs in InSAR processing (*Shen and Liu, 2020*).

One of the basic techniques for converting discrete data into continuous is interpolation. Interpolation is estimating the unsampled points using known values in sampled points and neighborhoods. The accuracy of the interpolation results depends on the spatial precision, the number and distribution of known points, and the models used. Optimal results are achieved when the characteristics of the mathematical model closely mirror the underlying patterns exhibited by the physical phenomenon under investigation. The objective of this study is to examine the contemporary crustal deformation pattern in the area of oblique collision between the Arabia-Eurasia tectonic plates, with the aim of providing a tectonic explanation.

Strain calculation could be done by different methods. The simplest method is Delaunay triangulation. The equations can be found, e.g., in *Cai and Grafarend (2007)*. Delaunay triangulation was generalized for spherical Earth by *Savage et al. (2001)*. Optimal interpolation of spatially discretized geodetic data for strain determination was done by *Shen et al. (2015)*. Seven additional configuration parameters are required to use this method, including distance weighting, either Gaussian or quadratic; spatial weighting, either azimuth or Voronoi cell; minimum, maximum, and incremental spatial smoothing constants; weighting threshold; and uncertainty threshold.

Biharmonic spline interpolation for one and two-dimensional data was proposed by *Sandwell (1987)*. It was developed by *Sandwell and Wessel (2016)* to interpolate two-dimensional vector data by considering the elastic relationship of the components. Their interpolation method for two-dimensional vector data uses constraints from elasticity. The present study utilizes a thin-sheet elastic interpolation scheme as its basis. To successfully employ this approach, three supplementary configuration parameters, namely Poisson ratio, fudge factor, and part of small eigenvalues that are removed from smoothing, are required. *Handwerger et al. (2019)* utilizes the weighted nearest neighbor algorithm. To utilize this method, two more configuration parameters, namely the radius of the search neighborhood and the minimum number of stations within the search radius, are mandatory. Multiscale estimation of GPS velocity fields using spherical wavelets was done by *Tape et al. (2009)*. Kriging is an interpolation method founded on conventional geostatistical analysis that entails the specification of a model type and three parameters. The model type denotes the

correlation structure of the underlying field and can be one of the three: a white-noise "Nugget" model, a continuous yet non-differentiable "exponential" model, or a continuous and differentiable "Gaussian" model. In order to construct models, a fundamental component known as a nugget is necessary. This represents the level of variability in observations at specific points, which in the case of GNSS velocities is equivalent to data uncertainty. The Gaussian and exponential models require additional parameters, namely the "sill" and "range". The former specifies the overall average variability in the dataset and should be determined as the total variance of the observations, minus the nugget. It should be noted that the nugget can be viewed as the variance of data uncertainties, while the sill represents the variance of the data itself. The range signifies the isotropic spatial correlation length scale (*Wu et al., 2017*). *Cardozo and Allmendinger (2009)* use grid-nearest neighbor and grid-distance weighted methods to calculate strain rate from a horizontal GPS velocity field. Strain rate tensor in Iran was calculated from GPS measurements by *Masson et al. (2007)* using the Delaunay triangulation method. *Masson et al. (2014)* calculated the strain rate tensor in Iran from the GPS velocity field using temporal variations of the baseline components.

We used biharmonic splines based on Green functions to interpolate the 369 horizontal GPS velocity field data from 1997 to 2015 in the oblique collision zone of the Arabia-Eurasia tectonic plates. According to *Sandwell and Wessel (2016)*, the root mean square misfit of the interpolated velocity for a Poisson ratio value of 0.5 is minimum. Therefore, we did a coupled interpolation with a Poisson ratio of 0.5 and obtained the uniform velocity field and strain rate field with a grid of 30′.

In Section 2, we introduce the GPS velocity field used in this paper and review the velocity field interpolation and strain calculation methods used. In Section 3, velocity field interpolation is described in detail. First, the trend is fitted to the input data. The difference between the actual data and the trend values will give the residuals. Then we do a reduction of residual values and finally fit the spline to the residuals. Then we do predictions on the grid and add them to the trend. In Section 4, we describe the movement patterns and strain distribution of the Arabia-Eurasia oblique collision zone based on our interpolated velocity field. Finally, in Section 5, we give the conclusions of this paper. The interpolated velocity field shows several large undeformed regions, strain focused around some major faults and regions of compressed strain. In general, it confirms the compression of the high plateau.

## *2.* DATA AND METHODS

### 2.1. Data

To perform the gridding process, we utilized the latest and comprehensive unified GPS velocity field for the oblique collision zone of the Arabia-Eurasia tectonic plates in Eurasia-fixed reference frame (Fig. 1). The Eurasia-fixed reference frame coordinates are established according to the definition of the Eurasia plate provided by *Altamimi et al. (2013)*. This GPS velocity field is derived from the combination of data collected over a span of 10 years (2006–2015) from the Iranian Permanent GNSS Network (IPGN). It combines these recent observations with previously published velocity solutions obtained from GPS survey measurements conducted between 1997 and 2013 (*Khorrami et al., 2019*). There are a total of 398 horizontal GPS velocity records included in the dataset.

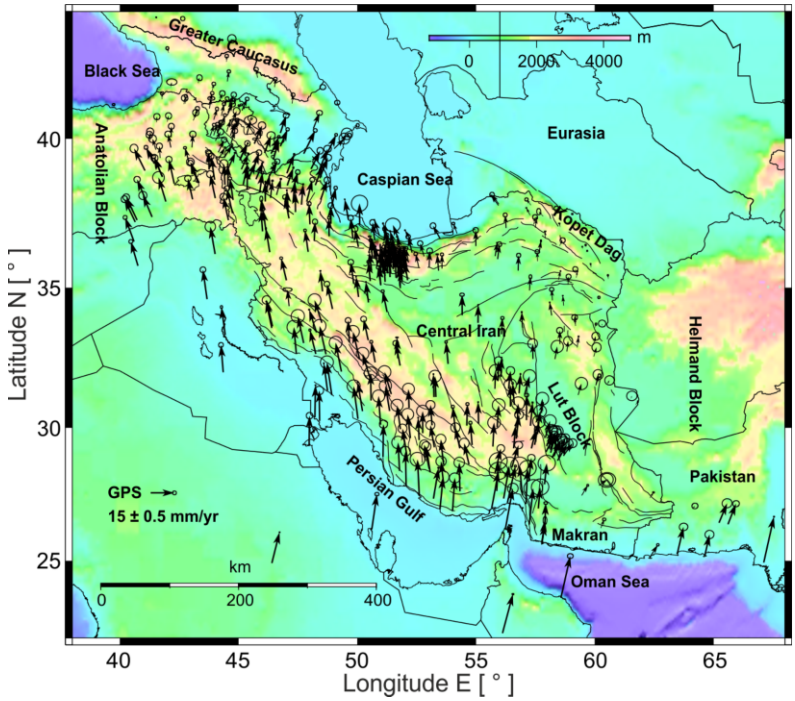


**Fig. 1.** Horizontal GPS velocity field in the Eurasia fixed reference frame from *Khorrami et al. (2019)* used for interpolation. Velocity fields are adapted from *Reilinger et al. (2006)*, *Frohling and Szeliga (2016)*, *Raeesi et al. (2017)* and Iranian Permanent GNSS Network. Major active faults in Iran, East Turkey, and the Caucasus are adapted from *Hessami et al. (2003)*, *Ghods et al. (2015)*, and *Talebian et al. (2013)*.

Figure 2 displays the spatial distribution of GPS stations in terms of longitude and latitude, accompanied by the color-coded representation of the eastern (Fig. 2a) and northern (Fig. 2b) velocity components magnitude. The range of velocities for the eastern component ranges from −6.91 to 12.64 mm $yr^{-1}$, while for the northern component, it ranges from −3.04 to 29.03 mm $yr^{-1}$.

## 2.2. Interpolation methods

The main objective of interpolation is to obtain a continuous strain rate field of the crust using discrete GPS velocity data. One possible approach for gridding vector data involves independently gridding individual components. Alternatively, we can perform coupled or joint gridding of two components by incorporating them using elastic deformation theory. In this study, we utilized both interpolation methods separately. To perform the interpolation, the first step involves estimating the trend of the input data using the least squares method. The difference between the actual data and the trend values represents the residuals. Then the residual values are reduced and finally the spline is fitted on the residuals. Following that the prediction is done on the grid, which is subsequently merged

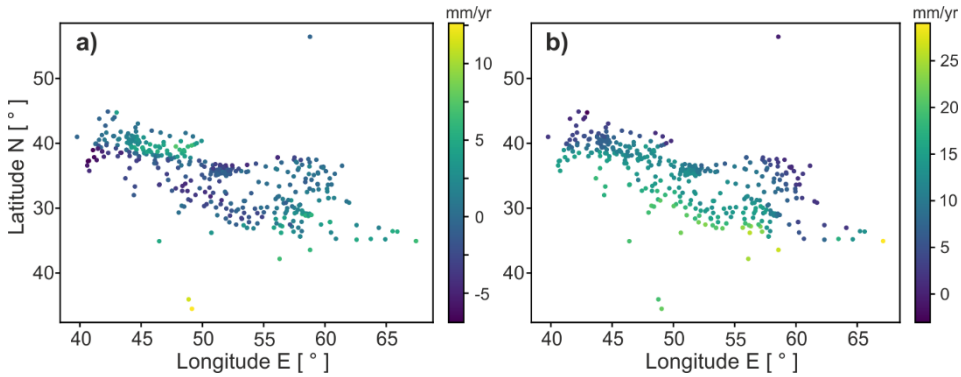


**Fig. 2.** Scatterplots of the GPS stations according to longitude and latitude in degrees, along with **a)** eastern and **b)** northern components of the velocity field.

with the trend. The procedure, which encompasses the steps of reduction, calculation, and recovery, is widely practiced in the field of geodesy.

### 2.2.1. Green functions

This methodology is well-suited, although not exclusively limited, to data that exhibit elastic or semi-elastic deformation, such as horizontal GPS velocities. The approach relies on utilizing the Green functions method of two-dimensional vector data based on elastic deformations, as proposed by *Sandwell and Wessel (2016)*, for data-coupled interpolation. This approach assumes two dimensional Cartesian coordinates and interpolates the data by estimating point forces that generate an elastic deformation that corresponds to the observed vector data. The deformation equations are derived from a two-dimensional elastic sheet with a constant Poisson ratio, and the data can be predicted at any desired location. The Earth's surface can be considered as two-dimensional, making the planar sheet model appropriate. Also, the Earth exhibits elastic mechanical properties and deforms under the influence of various forces, for which the elastic model is suitable. So, the underlying assumptions of this approach are well-suited for the Earth's surface. The eastern and northern components of the data are interrelated through the elastic deformation equations, which are influenced by the Poisson ratio, typically ranging between –1 and 1.

Our objective is to compute the two-dimensional displacement vector

$$\boldsymbol{u}(x,y) = u_x(x,y)\,\boldsymbol{i} + u_y(x,y)\,\boldsymbol{j}$$

caused by a two-dimensional in-plane body force vector. The quasi-static force balance equations in two-dimensions were developed by *Haines et al. (2015)* as follows:

$$\begin{aligned} &\frac{2}{1-\nu}\frac{\partial^2 u_x}{\partial x^2} + \frac{2\nu}{1-\nu}\frac{\partial^2 u_y}{\partial x\,\partial y} + \frac{\partial^2 u_x}{\partial y^2} + \frac{\partial^2 u_y}{\partial x\,\partial y} = -\frac{f_x}{\mu}\delta(x)\delta(y), \\ &\frac{\partial^2 u_x}{\partial x\,\partial y} + \frac{\partial^2 u_y}{\partial x^2} + \frac{2\nu}{1-\nu}\frac{\partial^2 u_x}{\partial x\,\partial y} + \frac{2}{1-\nu}\frac{\partial^2 u_y}{\partial y^2} = -\frac{f_y}{\mu}\delta(x)\delta(y). \end{aligned} \tag{1}$$

Here $\nu$ denotes Poisson ratio, $\mu$ represents the shear modulus, and $f_x$, $f_y$ denote the corresponding components of vector of force. The force per unit distance is the designated unit, and at a specific point, forces are applied using the two-dimensional delta function $\delta(x)\delta(y)$. The most straightforward approach to solve this problem involves applying the two-dimensional Fourier transform to Eq. (1). As a result of the transformation, the equations are modified as follows:

$$\begin{bmatrix} \frac{2}{1-\nu}k_x^2 + k_y^2 & \frac{1+\nu}{1-\nu}k_x k_y \\ \frac{1+\nu}{1-\nu}k_x k_y & \frac{2}{1-\nu}k_y^2 + k_x^2 \end{bmatrix} \begin{bmatrix} U_x(\boldsymbol{k}) \\ U_y(\boldsymbol{k}) \end{bmatrix} = \frac{1}{4\pi^2\mu} \begin{bmatrix} f_x \\ f_y \end{bmatrix}. \tag{2}$$

Here, $k_x$ and $k_y$ are wave numbers, defined as the reciprocal of the respective wavelength; $U_x$ and $U_y$ are displacement components in Fourier domain. In order to obtain the response resulting from a point force, it is necessary to invert this set of equations and perform the inverse 2-D Fourier transform of the resulting expression. The inverse of the matrix is given by:

$$\begin{bmatrix} U_x(\boldsymbol{k}) \\ U_y(\boldsymbol{k}) \end{bmatrix} = \frac{1}{8\pi^2\mu k_r^4} \begin{bmatrix} 2k_r^2 - (1+\nu)k_x^2 & -(1+\nu)k_x k_y \\ -(1+\nu)k_x k_y & 2k_r^2 - (1+\nu)k_y^2 \end{bmatrix} \begin{bmatrix} f_x \\ f_y \end{bmatrix}, \tag{3}$$

where $k_r^2 = k_x^2 + k_y^2$. It should be noted that in the specific case where the Poisson ratio is equal to −1, the solution undergoes simplification and can be expressed as follows:

$$\begin{bmatrix} U_x(\boldsymbol{k}) \\ U_y(\boldsymbol{k}) \end{bmatrix} = \frac{1}{4\pi^2\mu k_r^2} \begin{bmatrix} 1 & 0 \\ 0 & 1 \end{bmatrix} \begin{bmatrix} f_x \\ f_y \end{bmatrix}. \tag{4}$$

This corresponds to interpolation where there is no interaction between the two velocity components, and the Green function is denoted by:

$$\phi(\boldsymbol{r}) = \|\boldsymbol{r}\|^2 \left(\log\|\boldsymbol{r}\| - 1\right), \tag{5}$$

and the two components of GPS velocities are treated as independent and interpolated separately. The general solution relies on the three functions in Eq. (3):

$$Q(\boldsymbol{k}) = \frac{2k_r^2 - (1+\nu)k_x^2}{k_r^4}, \quad P(\boldsymbol{k}) = \frac{2k_r^2 - (1+\nu)k_y^2}{k_r^4}, \quad W(\boldsymbol{k}) = \frac{-(1+\nu)k_x k_y}{k_r^4}. \tag{6}$$

In order to obtain the solution in the spatial domain, it is necessary to evaluate the 2-D inverse Fourier transform of the following four component functions:

$$F_2^{-1}\left[\frac{1}{k_x^2 + k_y^2}\right], \quad F_2^{-1}\left[\frac{k_x^2}{\left(k_x^2 + k_y^2\right)^2}\right], \quad F_2^{-1}\left[\frac{k_y^2}{\left(k_x^2 + k_y^2\right)^2}\right], \quad F_2^{-1}\left[\frac{k_x k_y}{\left(k_x^2 + k_y^2\right)^2}\right]. \tag{7}$$

The inverse transforms of these four functions can be directly obtained, leading to the following results:

$$-\ln r\,,\quad \frac{1}{2}\left[\frac{y^2}{r^2}-\ln r\right],\quad \frac{1}{2}\left[\frac{x^2}{r^2}-\ln r\right],\quad -\frac{1}{2}\frac{xy}{r^2}\,. \tag{8}$$

In the spatial domain, the three Green functions, as defined by Eq. (6), can be expressed as follows:

$$\begin{aligned} q(\boldsymbol{r}) &= 4\ln r+(1+\nu)\left(\frac{y^2}{r^2}-\ln r\right)=(3-\nu)\ln r+(1+\nu)\frac{y^2}{r^2}\,,\\ p(\boldsymbol{r}) &= (3-\nu)\ln r+(1+\nu)\frac{x^2}{r^2}\,,\\ w(\boldsymbol{r}) &= -(1+\nu)\frac{xy}{r^2}\,. \end{aligned} \tag{9}$$

The validity of the Green functions can be established by verifying that they satisfy the original differential equation (1).

In the following, description of the used numerical method is presented. Our objective is to calculate a vector velocity field that is smooth and accurately represents a finite set of $N$ measured vectors $\boldsymbol{u}_x(\boldsymbol{r}_i)$, $\boldsymbol{u}_y(\boldsymbol{r}_i)$. The vectors are associated with specific locations denoted by $\boldsymbol{r}_i=(x_i, y_i)$. To achieve the objective, we solve for a set of $N$ vector body forces, denoted as $\boldsymbol{f}_x^i$ and $\boldsymbol{f}_y^j$, which are applied at the locations corresponding to the velocity measurements. To determine the intensity of the body forces, we perform an inversion on a linear system of equations with dimensions $2N\times 2N$. The system is given by:

$$\begin{bmatrix}\boldsymbol{u}_x(\boldsymbol{r}_i)\\ \boldsymbol{u}_y(\boldsymbol{r}_i)\end{bmatrix}=\begin{bmatrix}\boldsymbol{q}(\boldsymbol{r}_i-\boldsymbol{r}_j) & \boldsymbol{w}(\boldsymbol{r}_i-\boldsymbol{r}_j)\\ \boldsymbol{w}(\boldsymbol{r}_i-\boldsymbol{r}_j) & \boldsymbol{p}(\boldsymbol{r}_i-\boldsymbol{r}_j)\end{bmatrix}\begin{bmatrix}\boldsymbol{f}_x^j\\ \boldsymbol{f}_y^j\end{bmatrix}. \tag{10}$$

Finally, the vector velocity field can be calculated at any desired location using the following equations:

$$\begin{aligned} \boldsymbol{u}_x(\boldsymbol{r}) &= \sum_{j=1}^{N}\left[\boldsymbol{q}(\boldsymbol{r}-\boldsymbol{r}_j)\boldsymbol{f}_x^j+\boldsymbol{w}(\boldsymbol{r}-\boldsymbol{r}_j)\boldsymbol{f}_y^j\right],\\ \boldsymbol{u}_y(\boldsymbol{r}) &= \sum_{j=1}^{N}\left[\boldsymbol{w}(\boldsymbol{r}-\boldsymbol{r}_j)\boldsymbol{f}_x^j+\boldsymbol{p}(\boldsymbol{r}-\boldsymbol{r}_j)\boldsymbol{f}_y^j\right]. \end{aligned} \tag{11}$$

The Verde package was used for data processing. It is a part of the Fatiando a Tera project (*https://www.fatiando.org/*). It is a package for spatial data processing and gridding using Green functions, or splines. This package is suitable for the spatial processing of GPS campaign observations as well as their interpolation in a way that is more meaningful than

nearest neighbor interpolation. The basic idea behind it is to blend machine learning with geospatial processing. It provides an interface between machine learning-style prediction and interpolation in geospatial science (*Uieda, 2018*).

#### 2.2.2. Strain rate calculation

If we consider the crust as an elastic body, we can calculate the strain or strain rate based on the observed displacement or velocity. The strain tensor for the Earth's surface can be defined as the partial derivative of displacement with respect to spherical coordinates (*Arnoso et al., 2020*). The calculation of strain rate can be classified into two methods: the segment approach and the gridded approach. The segment approach divides the study area into multiple segments, where subnets are used as the fundamental unit to calculate the strain parameters for each individual segment. Ultimately, the individual outcomes are combined to determine the uniform strain rate across the subnet. For instance, *Savage and Gan (2001)* utilized the Taylor series expansion formula for spherical displacement and strain to compute the strain rates of various blocks in the northwestern region of the United States. Additionally, the Delaunay triangulation method represents a common example of the segment approach (*Wdowinski et al., 2007*). Nevertheless, the drawbacks of these methods are apparent. In general, the absence of data redundancy prevents the detection and removal of outliers. Furthermore, the resulting strain rates from these methods exhibit discontinuities.

The gridded approaches divide the study area into uniform grids. Initially, the displacement function of all stations is fitted into a single displacement field function, followed by the calculation of the partial derivative at the grid point to directly obtain the distribution of the strain field. The calculation of displacement in gridded approaches primarily relies on statistical analysis. The gridded approaches encompass various methods, such as the multi-quadric function method, spherical harmonic function method, and least square collocation method (*Hackl et al., 2009*; *Shen et al., 2005*). The suitability of these strain calculation methods varies depending on the specific research objectives and the availability of data. Nevertheless, all of them are well-suited for inversion problems. As an example, *Shen et al. (2005)* employed the least square collocation method to solve for the strain rate at grid points in the California area, using weighted velocity field data based on the distance from the measuring point. In another approach, *Hackl et al. (2009)* projected the velocity field parallel and perpendicular to the fault, applied spline curve interpolation using Green function to create a uniform grid, and then calculated the strain rate field in the southern California region of the United States by taking the derivative of the spline function.

We employed the strain rate calculation method proposed by *Hackl et al. (2009)*, which involves determining the velocity gradient through the spatial partial derivative of the interpolated velocity field. By applying this method, we successfully obtained the strain rate component. Subsequently, the derivatives along the local north and east directions were computed to generate four continuous fields, which collectively represent a continuous strain rate tensor through a linear combination. Under the assumption of small deformations, the calculation of the strain rate tensor component is determined according to (also in *Hackl et al., 2009*):

$$\begin{cases} \varepsilon_{\varphi} = \dfrac{\partial u_{\varphi}}{\partial x_{\varphi}}, \\ \varepsilon_{\lambda} = \dfrac{\partial u_{\lambda}}{\partial x_{\lambda}}, \\ \varepsilon_{\varphi\lambda} = \dfrac{1}{2}\left( \dfrac{\partial u_{\lambda}}{\partial x_{\varphi}} + \dfrac{\partial u_{\varphi}}{\partial x_{\lambda}} \right). \end{cases} \tag{12}$$

Here, the symbols $\varphi$, $\lambda$, $u_{\lambda}$, and $u_{\varphi}$ correspond to latitude, longitude, velocity along the longitude direction, and velocity along the latitude direction, respectively. Additionally, $\varepsilon_{\varphi}$, $\varepsilon_{\lambda}$, and $\varepsilon_{\varphi\lambda}$ represent the three independent components of the strain rate tensor.

Equation (12) is used to calculate the maximum and minimum principal strains:

$$\begin{cases} \varepsilon_{max} = \dfrac{1}{2}\left[ \varepsilon_{\varphi} + \varepsilon_{\lambda} + \sqrt{\left( \varepsilon_{\varphi} - \varepsilon_{\lambda} \right)^2 + 4\varepsilon_{\varphi\lambda}^2} \right], \\ \varepsilon_{min} = \dfrac{1}{2}\left[ \varepsilon_{\varphi} + \varepsilon_{\lambda} - \sqrt{\left( \varepsilon_{\varphi} - \varepsilon_{\lambda} \right)^2 + 4\varepsilon_{\varphi\lambda}^2} \right], \end{cases} \tag{13}$$

where $\varepsilon_{max}$ denotes the maximum principal strain, and $\varepsilon_{min}$ the minimum principal strain.

The determination of the maximum shear strain rate and its direction can serve as a valuable tool in identifying active faults, as the movement along a fault is typically accompanied by shear stress on the geological structure. In the event of an earthquake, a fault oriented in this direction has the highest likelihood of rupture. The maximum shear strain rate at each grid point can be calculated through a linear combination of the maximum eigenvalue and the minimum eigenvalue. Equation (13) is used to calculate the maximum shear strain rate $\varepsilon_{max\_shear}$:

$$\varepsilon_{max\_shear} = \frac{1}{2}\left( \varepsilon_{max} - \varepsilon_{min} \right). \tag{14}$$

The representative measure of horizontal deformation associated with the dip-slip fault is the dilation rate $\delta$ (*Fossen, 2016*):

$$\delta = \varepsilon_{max} + \varepsilon_{min}. \tag{15}$$

Next, the rotation rate, $\varepsilon_{rot}$, is defined as:

$$\varepsilon_{rot} = \frac{1}{2}\left( \frac{\partial u_{\lambda}}{\partial x_{\varphi}} - \frac{\partial u_{\varphi}}{\partial x_{\lambda}} \right). \tag{16}$$

The energy characteristics of regional crustal deformation are reflected by the second strain rate invariant, $\varepsilon_{second\_inv}$, calculated as:

$$\varepsilon_{second\_inv} = \sqrt{\varepsilon_{max}^2 + \varepsilon_{min}^2}. \tag{17}$$

## 3. RESULTS

Data with a long distance from the study area are not included in the grid because they do not contain much information. Therefore, the first step to take is to remove the data outside the region of 42°E as the western boundary, 66°E as the eastern boundary, 24°N as the southern boundary, and 42°N as the northern boundary. Thus, the data are cropped to the oblique collision zone of the Arabian-Eurasian tectonic plates. Thus, 398 GPS data points were cropped to the study area and reduced to 365. This is what we are going to grid and analyze.

### 3.1. Map projection

The Green functions used in this research have been developed for the half-space environment. Hence, the geodetic longitude and latitude grid should be converted to a Cartesian grid. For this purpose, we used a Mercator map projection with the mean latitude of campaign data as the latitude of true scale. Choosing the Mercator map projection is optional, and other map projections can be used as well.

### 3.2. Detrending

If there is a strong trend in the data, the spline can struggle to recover the long wavelength trends. It will be useful if we remove the trend first then grid the residuals and finally restore the trend. Thus, the first step is detrending. A quadratic two-dimensional polynomial is fitted to the eastern and northern components of the GPS velocity field (Fig. 3) and is removed from the data as a trend. The difference between the actual data and the trend values will give the residuals (Fig. 4).

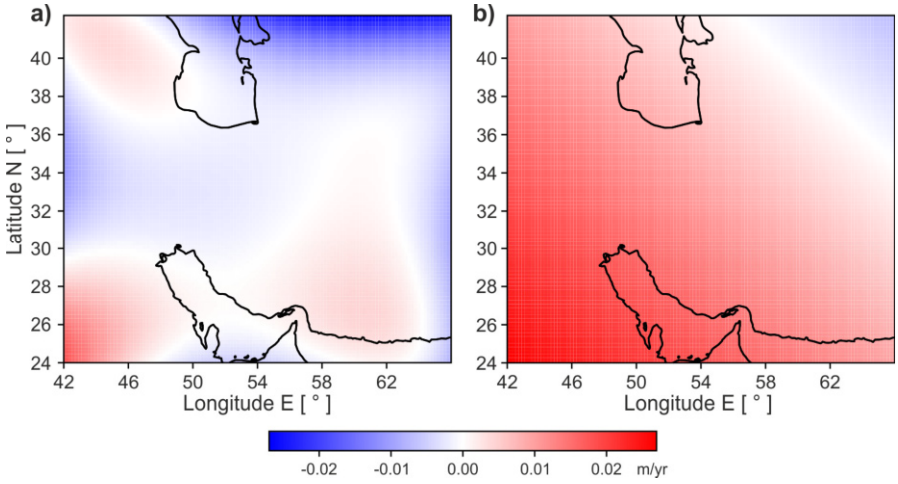


**Fig. 3.** Quadratic two-dimensional polynomial trend for **a)** eastern and **b)** northern components of the GPS velocity field.

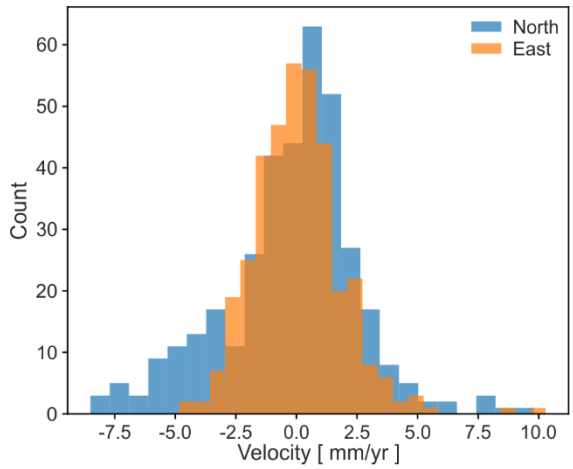


**Fig. 4.** Distribution of trend residuals for eastern and northern components, shown in Fig. 3.

### 3.3. Blocked reductions

With block reduction, the number of residuals will be lower. Splines will be fitted on the block to reduce residuals. The reason for the block reduction of data is that GPS stations are dense near big cities like Tehran and are very sparse in other areas. Therefore, we have a bias in the sampling, and if we make a gridded product of this data, it can produce aliasing effects in the final grid. We need to get rid of that to not bias the final grid. One way to do that is to actually throw away a little bit of data. Therefore, we have to somehow decimate the data. One way to do that is with a block reduction. In blocked reduction, we divide the whole region into blocks of a given size, and we apply the mean, the median, or some sort of reduction function to all the data points that are inside each block. The reduction function takes numbers inside a block and returns a single number. We used the median instead of the mean to do the reduction. The size of the blocks was chosen as 50 km. The number of data points was reduced from 365 to 262 by block reduction (Fig. 5). The advantages of block reduction from the numerical aspect are: (1) avoiding the effects of aliasing; and (2) converting all initial data into a small amount of data, which will lead to a faster run. We will get more and more accuracy if block reduction is done with smaller block sizes, but there is a limit, and like any other data science application, we have to investigate the data and the model that are available at the preprocessing step.

### 3.4. Gridding with splines

Green functions concept was used for gridding. The main idea behind it is that we create a linear model. This linear model is fitted to the data, and once the coefficients for the linear model are obtained, we can use them to make predictions about data anywhere. The model that we use is a thin elastic sheet. The data are forces pushing the sheet down, and the predictions are how much this sheet bends. So, there is a little bit of physics behind the type of splines used. We used a basic type of splines called biharmonic splines. They are very

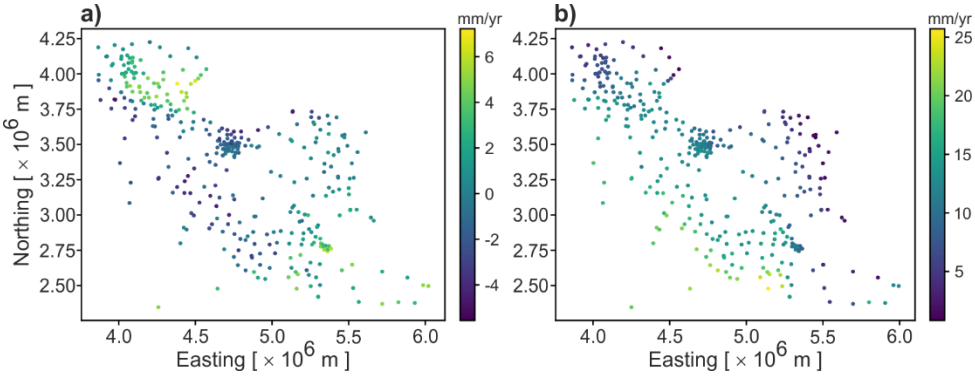


**Fig. 5.** Scatterplots of the blocked reduction results of the GPS stations according to Mercator projection for **a)** eastern and **b)** northern components of the velocity field.

good at interpolating points that are close to each other. But like other interpolation methods, they are not very good at distances very far away from observations.

The size of the model is going to be the same as the size of the dataset. So, what we are doing is basically a least squares regression with 262 parameters and data. This method is very powerful, but at the same time, it could be very costly for large data sets because we have to fit large linear models. For decimated data, it can be done very easily. We would need just $262 \times 262$ matrix inversion. We could predict values based on the actual observation points. It is important to note that unlike model fitting, prediction is done much faster. When we have a model, we can generate as many grids as we want at very little cost compared to fitting the model.

After making the prediction, the difference between the predictions and the real data, i.e., the residuals, is calculated. The residuals show how bad or wrong the prediction is at each point. Therefore, according to Fig. 6, it is possible to distinguish the places where the spline has overestimated or underestimated the data.

Figure 7 shows the histogram of residuals. According to Fig. 7, most of the residuals are close to zero. Most large residuals fall near active faults, and those are usually hard to recover with the spline. Hence, for the majority of our dataset, the spline is good at predicting it, but near active faults, it is not very good. It is important to note that this issue is prevalent across all interpolation methods.

Our main intention is to predict the velocity values at distinct locations. Suppose our intention is to predict these values on a regular grid with a spacing of 2 km. Figure 8 illustrates the outcomes following the restoration of trends.

As depicted by Fig. 8, the velocity field components have been expanded to encompass the entirety of the dataset coverage area, rather than being restricted solely to the GPS stations. The interpolated velocity field eastern component in the oblique collision zone of the Arabia-Eurasia tectonic plates is roughly zero, as demonstrated in Fig. 8a, and is also accompanied by a directional shift, indicating the presence of inflexible blocks in the collision zone. Additionally, Fig. 8b reveals that the northern component of the interpolated velocity field always has a positive value, supporting the notion of the Arabian plate shifting

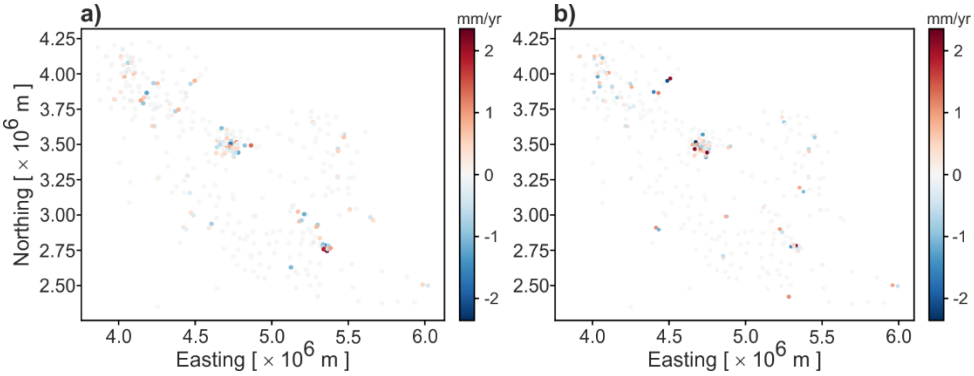


**Fig. 6.** Difference between predictions and the actual data for **a)** east and **b)** north velocity components of the GPS velocity field.

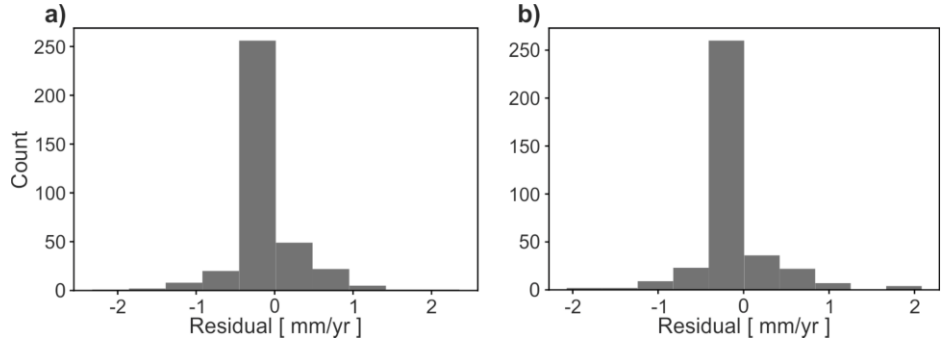


**Fig. 7.** Histogram of residuals for **a)** east and **b)** north velocity components of the data shown in Fig. 6.

towards Eurasia. The extent of the northern component's range is decreasing from south to north and from west to east.

As mentioned before, splines and other interpolation methods are not very good at predicting too far from the data. Based on this argument, the regions with a distance of more than 70 km from the data points were excluded from the gridding process (Fig. 9).

### 3.5. Model validation

To create the grid, a spline was fitted to the data, followed by the removal of regions that were located far from the data. The predictions are almost identical to the data used to fit the model, indicating that the model is at least good at retrieving the original data. Now, it is important to evaluate whether this result is considered satisfactory for gridding and assess the accuracy of interpolation. In order to address this problem, we will perform model validation to assess its performance.

The dataset is initially divided into training and testing subsets using a random partitioning approach. Afterward, the model is fitted to the training dataset, and its accuracy

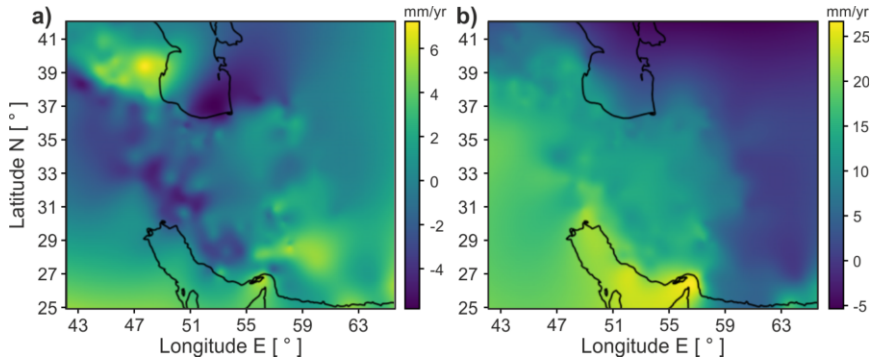


**Fig. 8.** Predicted **a)** eastern and **b)** northern components of the GPS velocity field on a regular grid with 2-km spacing.

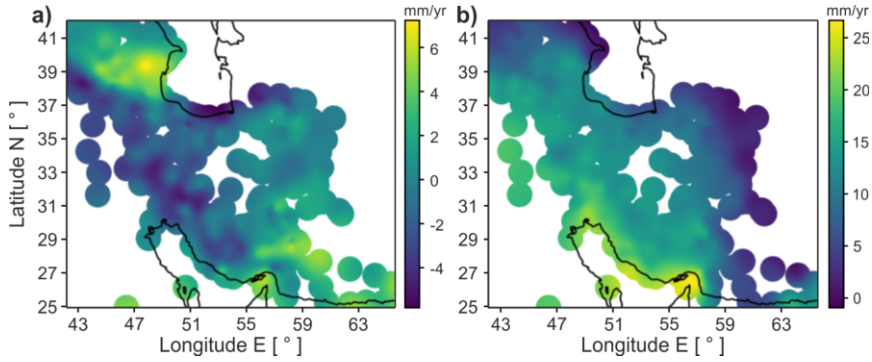


**Fig. 9.** **a)** East and **b)** north velocity components of the GPS velocity field. All the regions that are far away from our dataset (70 km) were masked.

is assessed by evaluating its performance on the testing dataset. A subset comprising 10% of the original data was randomly split for testing objectives. Predictions were made for the test data using the corresponding coordinates. The estimation of the goodness of fit involves calculating the coefficient of determination ($R^2$) on the provided testing data:

$$R^2 = 1 - \sum_{i=1}^{n} \left( u_i - \hat{u}_i \right)^2 , \tag{18}$$

where $\hat{u}_i$ is the interpolated velocity component.The coefficient of determination has a maximum value of one, indicating a perfect fit or an ideal quality fit. However, there is no minimum value, which means it is possible to have a fit with extremely low quality. In this study, the $R^2$ values for the east and north velocity components are 0.78 and 0.93, respectively. These values indicate that the model achieves a remarkably good fit, particularly for north velocity components, and are indicative of highly accurate predictions for points where no observational data is available.

However, due to the random sampling of points, some of the testing points happen to be located very close to an observation. As a result, the $R^2$ value does not accurately represent interpolations that are far from the data points, creating a bias towards larger values. Considering the spatial autocorrelation of the data, where nearby GPS stations exhibit a tendency to possess highly similar values, it follows that making predictions at points in close proximity to the data points will naturally yield accurate results. Consequently, relying solely on the $R^2$ value for interpolation may lead to a false sense of security. To tackle this issue, blocked splitting can be employed as a solution. In this method, the data is partitioned into spatial blocks, each with a fixed size. Based on this method, the data were divided into spatial blocks with specific dimensions equal to 50 km. The first point that can be noticed is that the test points are not randomly distributed. All test points are grouped together in blocks with specific dimensions. Hence, employing the method of blocked splitting, the data is divided into distinct blocks, followed by a random division of these blocks into training and testing datasets. This ensures that, on average, the testing datasets are at least 50 km away from any training dataset. If we separate the training and testing datasets with different block spacing, it gives a different $R^2$ value. With 50-km spacing, the $R^2$ value is 0.56 and 0.81 for the eastern and northern velocity components, respectively, which is actually much lower than previous values, i.e., 0.78 and 0.93. These $R^2$ values are representative of predictions 50 km away from any observations. If we have a point that is 50 km away from any observations, the $R^2$ values that we can expect from it are closer to 0.56 than 0.78 for the eastern component and closer to 0.81 than 0.93 for the northern component. Therefore, when dealing with spatial data, it is very important to use block train-test sampling instead of random sampling. This method is also effective for performing machine learning-style validation for other types of spatial data. In both random and blocked sampling modes for interpolation validation, the $R^2$ values obtained for the northern components is better than the eastern components.

#### 3.5.1. Cross validation

Although blocked splitting shows the advantage of accuracy in interpolation, it is highly dependent on random split and therefore does not provide a comprehensive view of interpolation accuracy. It provides a single instance to assess the accuracy of interpolation. If, by luck of the draw, the test dataset includes data points that either indicate a lack of significant patterns or exhibit high smoothness, we may obtain a higher $R^2$ value than we would under different circumstances. To obtain a more comprehensive understanding of how the $R^2$ value fluctuates based on the allocation of datasets for training and testing, cross-validation is employed, which enables a more holistic depiction of the variations (*Roberts et al., 2017*).

We perform cross-validation using techniques commonly employed in machine learning. The cross-validation technique we employed is known as K-fold cross-validation (*Valavi et al., 2018*). Let assume that we are conducting three-fold cross-validation. We partition the dataset into three separate parts. Following that, one of these partitions will be allocated as the testing dataset, while the other two will be utilized as the training datasets. We perform training and scoring using $R^2$ as the metric, and subsequently, we switch the order of these procedures. Suppose we consider the first block for testing and the second and third blocks for training. Then, we will perform training on the first and third blocks

while utilizing the second block for testing. This process will be repeated until we have exhausted all possible permutations. When utilizing K-fold cross-validation, we can ensure that we cover the entire dataset by systematically alternating between training and testing. We performed a blocked k-fold cross-validation, where the dataset was divided into blocks with a spacing of 50 km. Generally, when we perform ten splits, it implies that each testing dataset will consist of 10% of the total data. One important thing is to shuffle the dataset because otherwise the blocks will all be bunched together. This process can be somewhat time-consuming since it involves dividing the data into ten parts, resulting in the fitting and scoring process being repeated ten times as well.

Figure 10 displays the $R^2$ score distributions for the eastern and northern components, respectively, based on the results of 10-fold cross-validation. As evident from these plots, it is apparent that a common coefficient of determination of 0.75 can be achieved. However, depending on the assigned folds, it is also feasible to obtain a significantly lower coefficient of determination, approximately 0.65. Conversely, a higher $R^2$ value, around 0.85, is also possible. Thus, this comprehensive representation provides a more complete understanding of the interpolation accuracy.

Also, the coupled interpolation of the block-reduced GPS velocity field was performed using a Poisson ratio of 0.5. The result of interpolation by removing all grid areas with a distance of more than 70 km from the dataset is shown in Fig. 11.

Validation was also done without and with block splitting. The value of $R^2$ for data without block splitting is 0.88, and with block splitting it is 0.84. Also, 10-fold cross-validation was done with a block size of 50 km.

According to Fig. 12, it can be observed that a coefficient of determination of approximately 0.77 is commonly obtained during the interpolation of the components. However, the allocation of blocks can lead to the acquisition of a higher $R^2$, around 0.90, or a lower one, approximately 0.65.

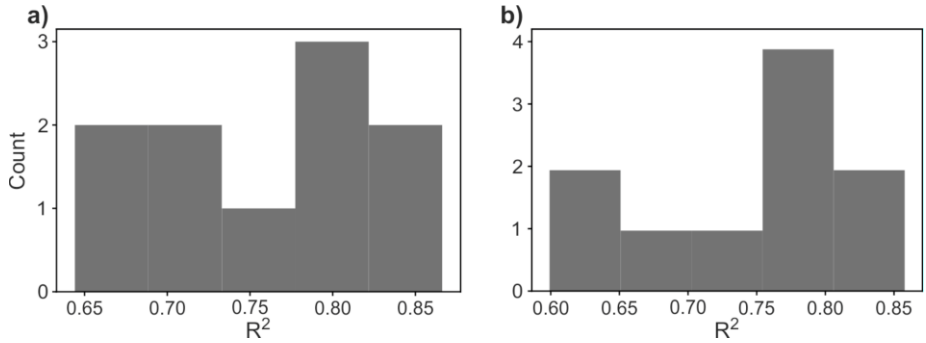


**Fig. 10.** Coefficient of determination $R^2$ for **a)** eastern and **b)** northern components of the GPS velocity field based on the results of 10-fold cross-validation.

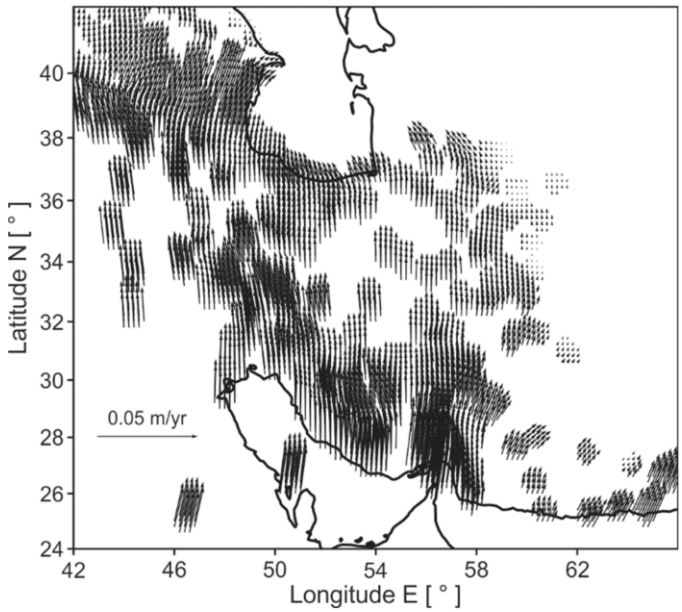


**Fig. 11.** Interpolation of two components of the GPS velocity field, that were coupled through Poisson ratio.

## 4. TECTONIC FEATURES OF THE INTERPOLATED VELOCITY FIELD

Here, we present an analysis of gridded velocity field for the oblique collision zone of Arabia and Eurasia tectonic plates. The strain rate was estimated using the gridded velocity field and scalar quantities extracted from it. These estimates are consistent with the findings of several prior studies, including *Vernant and Chéry (2006)*, *Masson et al. (2014)*, *Khorrami et al. (2019)*, and *Rastbood (2023)*. The interpolated velocity field provides insight into the key features of deformation within the collision zone, as illustrated in Figs 13–18. Our examination of the velocity field reveals that deformation is not uniformly distributed within the region, but rather occurs predominantly within the Eurasian plate, with little significant deformation observed in the Arabian plate. Furthermore, we observe distinct regions within the velocity field that exhibit low strain rates in their interiors, but higher strain rates around their boundaries. These non-deforming regions are clearly delineated from the surrounding deforming regions, as depicted in Fig. 16.

One remarkable feature of interpolated velocity field is the concentration of tension in proximity to particular major faults situated within the region. The North Tabriz Fault, Khazar, Mosha, Golbaf-Sirch, HZF, and Zendan-Minab faults, as shown in Figs 13 and 16, represent some of the most prominent among these. Although some major faults exhibit strain concentrations, another essential attribute of the interpolated velocity field for the collision zone is the existence of extensive areas of compressed strain, as evidenced in Figs 16 and 18. As demonstrated in Fig. 16, dilatation field indicates convergence in the Zagros and Alborz Mountain regions that is almost perpendicular to the convergence

direction. Furthermore, elevated strain rates for most areas in the oblique collision zone of the Arabia-Eurasia tectonic plates are demonstrated by the second invariant of the strain rate field, as seen in Fig. 17.

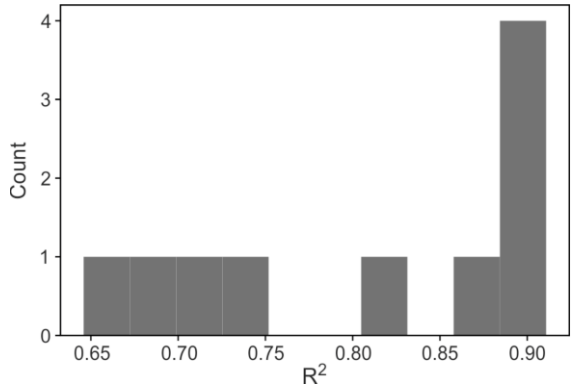


**Fig. 12.** Coefficient of determination $R^2$ for coupled interpolation of two components of the GPS velocity field based on the results of 10-fold cross-validation.

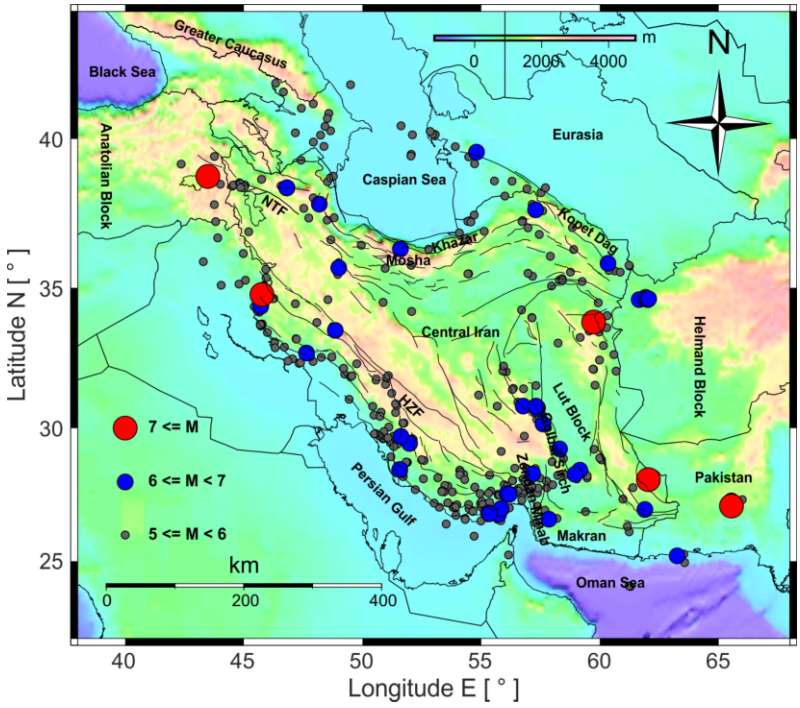


**Fig. 13.** Seismicity map for earthquakes with a magnitude greater than 5 for the study area based on the Iranian Seismologic Center (IRSC) catalog.

Comparison of dilatation, second invariant and maximum shear strain rate maps (Figs 16–18) with seismicity map (Fig. 13) indicates a potential correlation between strain rate and seismicity. This comparison provides observational correlations and can help in understanding the potential implications of strain accumulation on seismic activity in the studied region. Central Iran and Lut blocks depict low strain rate and low seismicity. On the other hand, there is a high correlation between high strain rate and high seismicity in Talash, Alborz, Kope Dag and Zagros. In these regions high strain values align with regions of high seismicity, indicating a potential correlation between strain accumulation and seismic activity. It is important to note that the comparison between calculated strain rate and seismicity maps provides valuable information but does not establish a direct causation between them. The correlation can vary depending on local geological complexities, temporal scales, and tectonic settings. Therefore, a comprehensive analysis that incorporates multiple lines of evidence is necessary to gain a more robust understanding of the relationship between strain rate and seismicity in a given area. The high strain rate and low seismicity of northwest Iran, taking into account the destructive historical earthquakes of the North Tabriz fault, shows the potential of severe earthquakes in this fault. Considering the limitations and uncertainties associated with both strain rate calculations and seismicity is necessary.

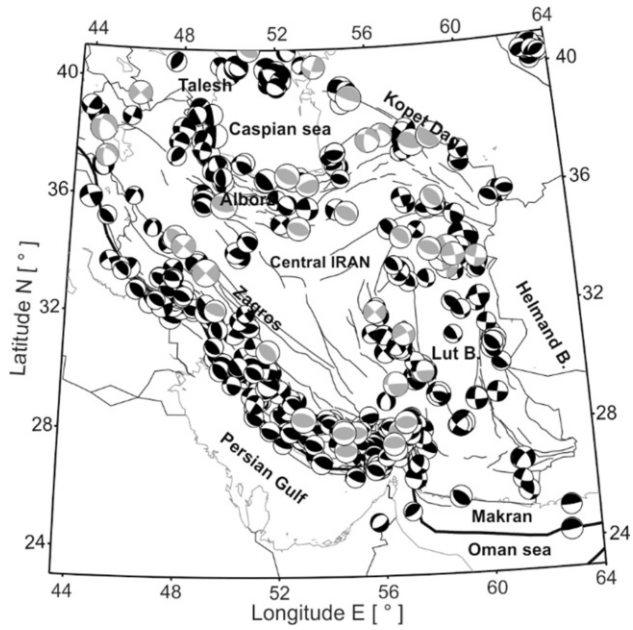


**Fig. 14.** Earthquake focal mechanisms in Iran between 1909 and 2011. The dark mechanisms are from the global CMT catalog and the light ones from *Jackson et al. (1995)*.

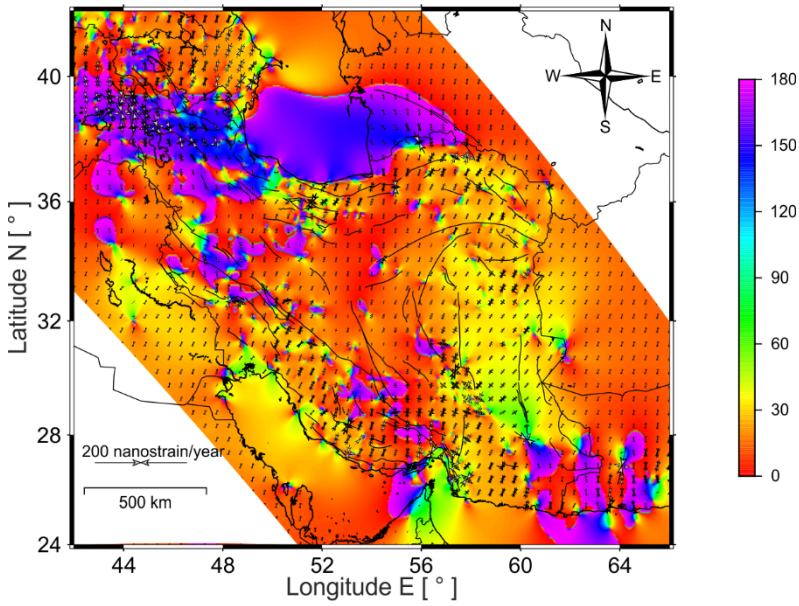


**Fig. 15.** Principal strain rate field. Bars indicate the principal compressional and extensional strain rates at the interpolation points. The background color shows the azimuth of maximum shortening in degrees from North.

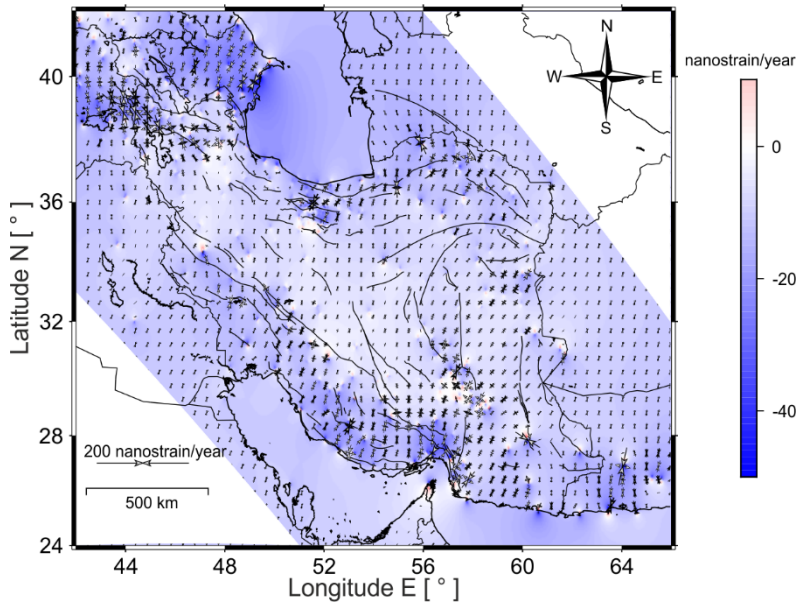


**Fig. 16.** Distribution of dilatational strain rate field. Crustal shortening is negative.

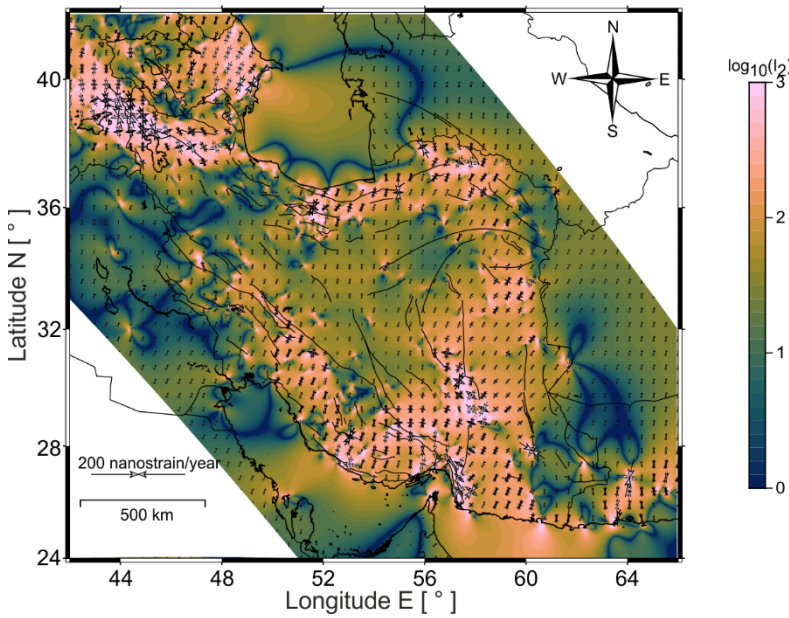


**Fig. 17.** Distribution of the $\log_{10}$ of second invariant of strain rate tensor $\mathbf{I}_2$.

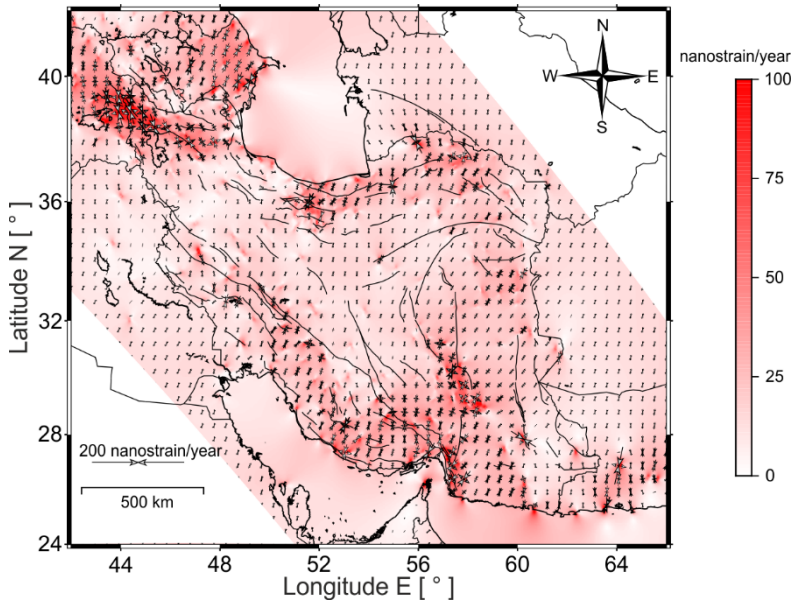


**Fig. 18.** Distribution of the maximum shear strain rate.

The comparison between strain and focal mechanisms requires careful interpretation. It is important to consider other geological and tectonic factors that may influence the observed patterns. Additionally, the resolution and accuracy of the data used for strain calculation and focal mechanism determination can affect the results. By comparing Fig. 14 with Figs 15–18 we can identify Zagros and Alborz regions with high strain and clustering of earthquakes with consistent focal mechanisms, so we can infer a potential relationship between strain accumulation and faulting patterns in these regions.

## 5. CONCLUSIONS

Accurate calculation of strain in the Earth's crust requires network densification and increased density of scattered GPS observations by interpolation. One approach to grid vector data is to grid each component separately. A different approach involves meshing the two components simultaneously, incorporating the interdependence of the components by leveraging the principles of elastic deformation theory. This method is particularly well-suited for datasets like GPS horizontal velocities, which indicate elastic or semi-elastic deformation. It offers valuable insights into how the interpolation behavior depends on various Poisson ratio values.

In cases where the deformation of the material follows the elastic equations, this approach offers enhanced interpolation capabilities for sparse vector data.

In this study, we employed biharmonic splines to interpolate the horizontal GPS velocity field data, which was sparsely represented by two-dimensional vectors, in the oblique collision zone of Arabia-Eurasia tectonic plates. The interpolation was carried out separately for each component and also in a coupled manner, relying on Green functions derived from elasticity constraints. In particular, Poisson ratio was set at 0.5, and the interpolation was conducted using 369 GPS station data points spanning from 1997 to 2015. As a result, we obtained a uniform velocity and strain rate field with a 30-minutes grid resolution.

To interpolate the sparse two-dimensional vector data from the horizontal GPS velocity fields, we utilized a two-step approach. First, we fitted a trend to the input GPS velocity field data using the least squares method, and then calculated the residuals by subtracting the predicted trend from the input data. The output was passed onto block reduction, which generated reduced data that was then passed onto a biharmonic spline. The spline was fitted on the residuals of trend fitting and block reduction, allowing for the prediction to be done in two steps - first by trend, then by spline - and added together. The trend and spline steps handled the long wavelengths and details in the grid, respectively, making it easier for the spline to perform well with long wavelengths.

The interpolation process involves remove, compute, and restore steps, which are common operations in geodesy. Finally, we conducted cross-validation to determine the model's validity. This method is particularly effective in improving the interpolation of scatter vector data when the deforming material follows the principles of elasticity equations.

The interpolated velocity field obtained from our study exhibits several key features that provide important insights into the crustal movement in the oblique collision zone of the Arabia-Eurasia tectonic plates. The spatial distribution of the crustal movement in this

region is found to be irregular and has distinct partitioning characteristics and with the range of the northern components of the velocity field being larger than that of the eastern components. Moreover, the direction of the northern component is consistently towards Eurasia, while the direction of the eastern component changes within the collision zone, pointing towards the west in the western half of Iran and more towards the east in the eastern half. However, in the northern regions of Iran, this trend is reversed. These characteristics are also reflected in the two-dimensional quadratic polynomial trend fitted to the eastern and northern components.

Further analysis reveals that the change in direction of the eastern component occurs as a block, which makes it possible to identify solid blocks within the collision zone. The amplitude of the northern component shows a decreasing trend from south to north and from west to east, while the amplitude of the eastern component in the inner regions of Iran is approximately zero, increasing from the center to the border of the collision zone. Interestingly, contrary to expectations, the increase in the eastern amplitude is considerable in the north and especially in the northwest of Iran.

Our research has enabled us to identify the existence of several extensive undeformed regions within the collision zone of Arabia and Eurasia. Certain significant faults can be observed in the velocity field as a result of strain concentrations. Furthermore, there are areas where convergence deformation is taking place, and the high-altitude regions of Zagros and Alborz are experiencing compression. Our study has yielded critical knowledge regarding the intricate movement and deformation patterns of the crust in this oblique collision zone. This understanding can have far-reaching implications in comprehending the tectonic evolution of this region.

In this paper, it is suggested that the interpolation of horizontal GPS velocity fields from local geodynamic networks can be utilized in estimating Poisson ratio values for optimal gridding validation. The study primarily focuses on interpolating two-dimensional GPS data, while three-dimensional GPS data gridding can be accomplished by utilizing the Green functions from prior studies conducted by *Uieda et al. (2018)* and *Uieda (2018)*. To grid different types of spatial data, the use of distinct Green functions is recommended. Additionally, future research should explore alternative interpolation methods for gridding the GPS velocity field, validating the outcomes with machine learning styles, and interpreting the results in a tectonic context.

*Acknowledgements:* All figures were drawn using the Generic Mapping Tools (*Wessel et al., 2019*).

*Preprint:* This paper has been preprinted on Research Square, *https://doi.org/10.21203/rs.3.rs-3203549/v1*

*References*

Arnoso J., Riccardi U., Benavent M., Tammaro U., Montesinos F.G., Blanco-Montenegro I. and Vélez E., 2020. Strain pattern and kinematics of the Canary Islands from GNSS time series analysis. *Remote Sens.*, **12**, Art.No. 3297, https://doi.org/10.3390/rs12203297

Cai, J. and Grafarend E.W., 2007. Statistical analysis of geodetic deformation (strain rate) derived from the space geodetic measurements of BIFROST project in Fennoscandia. *J. Geodyn.*, **43**, 214–238.

Cardozo N. and Allmendinger R.W., 2009. SSPX: A program to compute strain from displacement/velocity data. *Comput. Geosci.*, **35**, 1343–1357

Fossen H., 2016. *Structural Geology*. Cambridge University Press, Cambridge, U.K.

Frohling E. and Szeliga W., 2016. GPS constraints on interplate locking within the Makran subduction zone. *Geophys. J. Int.*, **205**, 67–76, https://doi.org/10.1093/gji/ggw001

Ghods A., Shabanian E., Bergman E., Faridi M., Donner S., Mortezanejad G. and Aziz-Zanjani A., 2015. The Varzaghan-Ahar, Iran, earthquake doublet (Mw 6.4, 6.2): implications for the geodynamics of northwest Iran. *Geophys. J. Int.*, **203**, 522–540

Gonzalez R.C. and Woods R.E., 2018. *Digital Image Processing*. 4th Edition, Pearson Education, New York, pp. 1022, ISBN 978-0-13-335672-4.

Hackl M., Malservisi R. and Wdowinski S., 2009. Strain rate patterns from dense GPS networks. *Nat. Hazards Earth Syst. Sci*., **9**, 1177–1187

Handwerger A.L., Huang M.-H., Fielding E.J., Booth A.M. and Bürgmann R., 2019. A shift from drought to extreme rainfall drives a stable landslide to catastrophic failure. *Sci. Rep.*, **9**, Art.No. 1569, https://doi.org/10.1038/s41598-018-38300-0

Haines A.J., Dimitrova L.L., Wallace L.M. and Williams C.A., 2015. *Enhanced Surface Imaging of Crustal Deformation: Obtaining Tectonic Force Fields Using GPS Data*. Springer Int. Publ., New York, https://doi.org/10.1007/978-3-319-21578-5

Hessami K., Jamali F. and Tabassi H., 2003. *Major Active Faults of Iran*. IIEES, Tehran, Iran

Jackson J., Haines J. and Holt W., 1995. The accommodation of Arabia-Eurasia plate convergence in Iran. *J. Geophys. Res.-Solid Earth*, **100(B8)**, 15205–15219

Khorrami F., Vernant P., Masson F., Nilfouroushan F., Mousavi Z., Nankali H., Saadat S.A., Walpersdorf A., Hosseini S., Tavakoli P., Aghamohammadi A. and Alijanzade M., 2019. An up-to-date crustal deformation map of Iran using integrated campaign-mode and permanent GPS velocities. *Geophys. J. Int.*, **217**, 832–843

Masson F., Anvari M., Djamour Y., Walpersdorf A., Tavakoli F., Daignieres M., Nankali H. and Van Gorp S., 2007. Large-scale velocity field and strain tensor in Iran inferred from GPS measurements: new insight for the present-day deformation pattern within NE Iran. *Geophys. J. Int.*, **170**, 436–440

Masson F., Lehujeur M., Ziegler Y. and Doubre C., 2014. Strain rate tensor in Iran from a new GPS velocity field. *Geophys. J. Int.*, **197**, 10–21

Raeesi M., Zarifi Z., Nilfouroushan F., Boroujeni S.A. and Tiampo K., 2017. Quantitative analysis of seismicity in Iran. *Pure Appl. Geophys.*, **174**, 793–833

Rastbood A., 2023. Multiscale analysis of GPS velocity fields in the oblique collision zone of Arabia-Eurasia tectonic plates using spherical wavelet. *J. Earth Space Phys.*, **49**, 541–565 https://doi.org/10.22059/jesphys.2023.340395.1007412

Reilinger R., McClusky S., Vernant P., Lawrence S., Ergintav S., Cakmak R., Ozener H., Kadirov F., Guliev I. and Stepanyan R., Nadariya M., Hahubia G., Mahmoud S., Sakr K., ArRajehi A., Paradissis D., Al-Aydrus A., Prilepin M., Guseva T., Evren E., Dmitrotsa A., Filikov S.V., Gomez F., Al-Ghazzi R. and Karam G., 2006. GPS constraints on continental deformation in the Africa-Arabia-Eurasia continental collision zone and implications for the dynamics of plate interactions. *J. Geophys. Res.-Solid Earth*, **111**, Art.No. B05411, https://doi.org/10.1029/2005JB004051

Roberts D.R., Bahn V., Ciuti S., Boyce M.S., Elith J., Guillera-Arroita G., Hauenstein S. Lahoz-Monfort J.J., Schröder B., Thuiller W., Warton D.I., Wintle B.A., Hartig F. and Dorman C.F., 2017. Cross-validation strategies for data with temporal, spatial, hierarchical, or phylogenetic structure. *Ecography*, **40**, 913–929

Sandwell D.T., 1987. Biharmonic spline interpolation of GEOS-3 and SEASAT altimeter data. *Geophys. Res. Lett.*, **14**, 139–142

Sandwell D.T. and Wessel P., 2016. Interpolation of 2-D vector data using constraints from elasticity. *Geophys. Res. Lett.*, **43**, 10703–710709

Savage J., Gan W. and Svarc J., 2001. Strain accumulation and rotation in the Eastern California Shear Zone. *J. Geophys. Res.-Solid Earth*, **106**, 21995–22007

Shen Z.K., Lü J., Wang M. and Bürgmann R., 2005. Contemporary crustal deformation around the southeast borderland of the Tibetan Plateau. *J. Geophys. Res.-Solid Earth*, **110**, Art.No. B11409, https://doi.org/10.1029/2004JB003421

Shen Z.K., Wang M., Zeng Y. and Wang F., 2015. Optimal interpolation of spatially discretized geodetic data. *Bull. Seismol. Soc. Amer.*, **105**, 2117–2127.

Shen Z.K. and Liu Z., 2020. Integration of GPS and InSAR data for resolving 3-dimensional crustal deformation. *Earth Space Sci.*, **7**, Art.No. e2019EA001036, https://doi.org/10.1029/2019EA001036

Talebian M., Ghorashi M. and Nazari H., 2013. *Seismotectonic Map of the Central Alborz*. Research Institute for Earth Sciences, Geological Survey of Iran, Tehran, Iran

Tape C., Musé P., Simons M., Dong D. and Webb F., 2009. Multiscale estimation of GPS velocity fields. *Geophys. J. Int.*, **179**, 945–971

Uieda L., 2018. Verde: Processing and gridding spatial data using Green functions. *J. Open Source Softw.*, **3**, Art.No. 957, https://doi.org/10.21105/joss.00957

Uieda L., Xu X., Wessel P. and Sandwell D.T., 2018. Coupled interpolation of three-component GPS velocities. Abstract. American Geophysical Union, Fall Meeting 2018, abstract #G23B-0587

Valavi R., Elith J., Lahoz-Monfort J.J. and Guillera-Arroita G., 2018. blockCV: An R package for generating spatially or environmentally separated folds for k-fold cross-validation of species distribution models. *Methods Ecol. Evol.*, **10**, 225–232, https://doi.org/10.1111/2041-210X.13107

Vernant P. and Chéry J., 2006. Low fault friction in Iran implies localized deformation for the Arabia-Eurasia collision zone. *Earth Planet. Sci. Lett.*, **246**, 197–206, https://doi.org/10.1016/j.epsl.2006.04.021

Wdowinski S., Smith-Konter B., Bock Y. and Sandwell D., 2007. Diffuse interseismic deformation across the Pacific-North America plate boundary. *Geology*, **35**, 311–314

Wessel P., Luis J.F., Uieda L., Scharroo R., Wobbe F., Smith W.H.F. and Tian D., 2019. The Generic Mapping Tools, Version 6. *Geochem. Geophys. Geosyst.*, **20**, 5556–5564, https://doi.org/10.1029/2019GC008515.

Wu Y., Jiang Z., Liu X., Wei W., Zhu S., Zhang L., Zou Z. Xiong X., Wang Q. and Du J., 2017. A comprehensive study of gridding methods for GPS horizontal velocity fields. *Pure Appl. Geophys.*, **174**, 1201–1217